ELSEVIER

Thermochimica Acta 370 (2001) 1–14

thermochimica acta

www.elsevier.com/locate/tca

Heat flux calorimetry in intermetallic compound–H_2(g) systems: heat measurements and modeling in the low pressures range

P. Dantzer*, P. Millet

CNRS-UMR 8647, bât 415, Université Paris Sud, 91405 Orsay Cedex, France

Received 6 November 2000; received in revised form 8 November 2000; accepted 12 November 2000

Abstract

A heat conduction calorimeter has been used to determine enthalpies of solid–gas reactions in systems, such as intermetallic compounds–H_2(g). It is shown that the significance of the heat measurements must be carefully analyzed by controlling several parameters, which may influence the heat transfer conditions during the absorption and desorption reactions.

For this type of reaction, the measured heat flow is strongly dependent on the heat transfers through the gas phase in the low pressure range (Knudsen regime). It is demonstrated, experimentally and confirmed with simple models, that heat measurements can provide erroneous enthalpies due to our inability to account for the unavoidable modifications of the heat losses in the transition region. Experiments were carried out on the ZrNi–H_2 system.

Keywords: Heat flux calorimetry; First order transition; Enthalpy; Heat transfer; Modeling; Intermetallic hydrides

1. Introduction

Calorimetric studies are currently performed in many fields of materials science, biology, chemistry, covering wide temperature and pressure domains. Since the first appearance of commercial heat flux (heat conduction) calorimeters in the 1960s, continuous improvements of the equipments have been made. Computer control of the calorimeter undoubtedly contributed to improve the accuracy of the measurements and also to simplify their use. More recently, additional techniques have been proposed in order to extend the application of thermal analysis in studies of materials, i.e. temperature modulated differential scanning calorimetry that is used to dynamic studies of reactions for which the transient thermal response of a sample excited by a variable heat input is directly dependent on the thermophysical properties of the material. Other extensions involve coupling of the calorimeter with a specific equipment for simultaneous studies of other properties, i.e. volumetric device with pressure measurements [1,2], mechanical traction device for stress, strain measurements [3], thermal desorption spectroscopy apparatus for studying the kinetics of decomposition of solid–gas reaction [4]. In parallel to these developments, commercial calorimeters benefit from powerful software packages that allow users to readily obtain data, although the data reduction in some cases is of doubtful quality. This is particularly true when the measurements are non-routine [5,6].

Calorimetry applied to the determination of enthalpies of phase transformation in intermetallic compound–H_2 systems falls into the non-routine class. This is shown by the conflicting results in the literature

* Corresponding author.
E-mail address: pierre.dantzer@lemhe.u-psud.fr (P. Dantzer).

0040-6031/01/$ – see front matter
PII: S0040-6031(00)00756-5

Nomenclature

a	accommodation factor used to calculate the equivalent H_2 thermal conductivity (dimensionless)
C	heat capacity (J kg^{-1} K^{-1})
g	temperature jump distance used to calculate the equivalent H_2 thermal conductivity
ΔH	relative molar enthalpy of phase transformation (kJ (mol H)$^{-1}$)
H/M	hydrogen to metal ratio (dimensionless)
k_c	calibration constant (J nV^{-1} s^{-1})
k_r	rate constant
k_v	Poiseuille's constant characterizing the needle valve
$n_1(t)$	number of mole of H_2 in the reference volume chamber (mol)
$n_2(t)$	number of mole of H_2 in the reactor (mol)
$n_H(t)$	number of mole of H absorbed by the sample (mol)
N	Johnson–Mehl–Avrami morphological parameter
P_1^0	initial pressure in the reference volume (Pa)
P_2^0	initial pressure in the reactor (Pa)
$P_1(t)$	time dependant pressure in the reference volume (Pa)
$P_2(t)$	time dependant pressure in the reactor (Pa)
R	ideal gas constant (8.314 Pa m^3 mol^{-1} K^{-1})
S	surface of heat exchange of the copper sample holder
S_{SS}	surface of heat exchange of the stainless steel guides
T_1	temperature in reference volume (K)
T_{HD}	temperature of the heat detector (K)
$T_s(t)$	temperature of the sample (K)
T_j	temperature above the sample (K)
V_1	calibrated reference volume (m^3)
V_j	partitioned volumes of the reactor (m^3)

Greek letters

α	transformed fraction of material for the $\alpha \rightarrow \beta$ phase transformation
$\lambda_{H_2}(T)$	temperature dependant thermal conductivity of gaseous hydrogen (J s^{-1} K^{-1} m^{-1})
$\lambda^*_{H_2}$	thermal conductivity of gaseous hydrogen in the low pressure domain (J s^{-1} K^{-1} m^{-1})
λ_{SS}	thermal conductivity of the stainless steel guides supporting fins and copper sample holder
δ	thickness of the gaseous film between the sample holder and the reactor wall
ϕ	thermal heat flux detected by the thermopiles (J s^{-1})

for seemingly identical systems. The discrepancies are mainly due to problems associated with hydrogen gas induced solid state transformation, as for a hydride formation reaction

$$(b-a)^{-1}\mathrm{MH}_a + \tfrac{1}{2}\mathrm{H}_2(\mathrm{plat,g}) \rightarrow (b-a)^{-1}\mathrm{MH}_b, \quad (1)$$

where MH_a and MH_b represent a solid solution and a hydride compound, respectively, and a, b correspond to the hydrogen contents at the phase boundaries.

Usually, the hydrided compound is a finely powdered material. An additional complicating feature is that the formation–decomposition of the hydride is accompanied by hysteresis that makes the thermodynamic behavior of these systems complex. In the two phase domain, reaction (1), the calorimeter measures an evolved heat of transformation that corresponds to a certain absorbed mass of hydrogen. The shape of the thermograms (not the integrated quantity), depends on the heat transfer conditions in the reactor. These conditions are influenced by the irreversible character of the transformation and by the morphology of the material. It follows that the meaning of the measured heat must be carefully analyzed taking into account the microstructural behavior and the low thermal conductivity of the powdered sample which can generate significant non-isothermal behavior within the sample. If isothermal conditions are not met, the thermodynamic path of the transformation is directly affected by different possibilities of coupling between hysteresis, temperature gradients and concentration gradients. In such cases the measured heat will certainly not represent the true heat of transformation, as can be seen from the calorimetric results reported by

Zhang et al. [7]. Thus, the priority in the thermodynamic characterization of intermetallic–H_2 systems is to determine the experimental parameters which will give isothermal conditions in the calorimeter and ensure homogeneous growth of the hydrided compound.

Assuming isothermal conditions and homogeneous growth, other problems can be generated by a non-appropriate use of the calorimeter that is related to the experimental conditions used. Such problems occur if the hydrogen pressure remains in the domain of the molecular regime (Knudsen domain). This problem is addressed in this paper where the thermodynamic characterization of an important intermetallic compound–H_2 system, ZrNi–H_2, has been made with a calorimeter coupled with a high precision volumetric device. The studies have been carried out over a wide temperature and pressure range to focus on the analysis of the calorimeter responses. Erroneous interpretation of these responses leads to erroneous enthalpy determination. Knowledge of accurate thermodynamic parameters are of paramount importance for any hydride application. The interest in the ZrNi–H_2 system is related to its possible use for hydrogen isotope storage, in separation technology [8,9], and its use in closed-cycle hydride cryocoolers [10].

The paper is organized as follows: after a brief overview on the ZrNi–H_2 system we give a short description of the experimental set-up and of the heat measurements which are obtained across the Knudsen domain. Next, simple models are developed to analyze the thermograms. These are based on coupling between the reaction itself and the induced heat transfer perturbation in the low pressure range.

2. The ZrNi–H_2 system

ZrNi was the first intermetallic compound investigated for its hydrogen absorption properties by Libowitz et al. [11] and later by Kost et al. [12]. The former authors observed a constant hydrogen plateau pressure from $H/Zr = 1$ to 2.7 at 373 K and the possible presence of another hydride. Westlake et al. [13] determined two structures corresponding to a triclinic monohydride phase, ZrNiH, and an orthorhombic trihydride phase, $ZrNiH_3$. The hydrogen site occupancy is rather peculiar since the tetrahedral interstices of the monohydride phase, with four Zr atoms as nearest neighbors, are empty in the trihydride phase where tetrahedral Zr_3Ni and pyramidal Zr_3Ni_2 interstices are occupied. Recent band structure calculations [14] have shown that in the ZrNiH phase, the preferred occupancy of the tetrahedral Zr_4 over the Zr_3Ni sites is associated with chemical effects rather than geometric factors such as hole size and H–H distances.

Since the early reports, the most extensive thermodynamic study of the system was carried out by Luo et al. [15]. The calorimetric measurements performed at 323 K and at hydrogen pressures corresponding to the first low plateau pressure, about 10^{-5} Pa, represent the only direct determination of the enthalpy of transformation of α to β ZrNiH. Recently, the temperature dependence of the enthalpy of transformation of β to γ $ZrNiH_{3-\delta}$ was determined by Dantzer et al. [16].

3. Experimental

3.1. The calorimeter–volumetric equipment

In order to maintain isothermal conditions and to ensure homogeneous growth of the hydrided compound, the coupling between the gas flow and the temperature variation within the sample must be controlled. This was successfully achieved in the present studies and details of the procedure, a full description of the equipment, as well as an analysis of the uncertainties in the measurements, are found in [1]. A schematic view of the computer-controlled apparatus is given in Fig. 1. The great stability of the signal delivered by the thermopiles, with fluctuations which do not exceed 4 nV, allows us to undertake calorimetric studies which require continuous operation of the equipment for about 10 days that may be needed for completion of an absorption–desorption loop. When operated under 'quasi-isothermal' conditions, the system allows steps in the H/M ratio from 0.003 (minimum dose for accurate heat detection) to 0.07 with maximum temperature rises at the sample level of 0.5°C.

3.2. Instrumentation of the reactor

The reactor consists of four parts: the head, the inner rod, the sample holder, and the chamber body. The

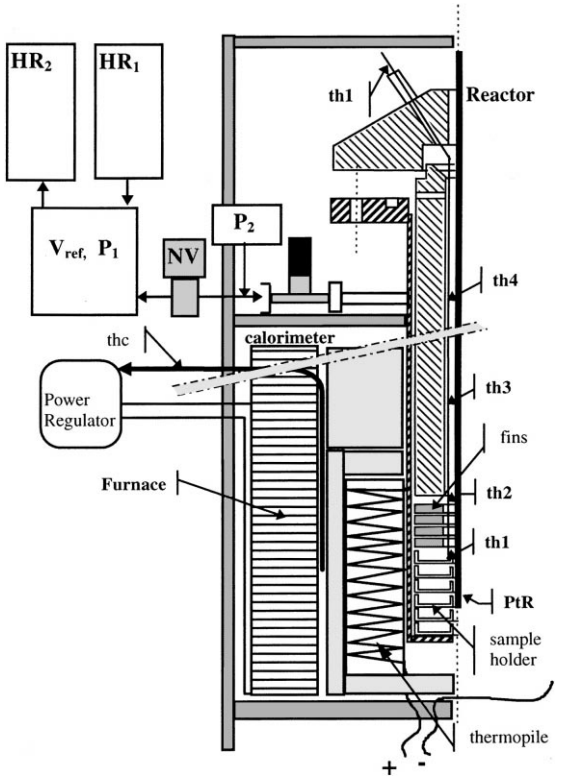

Fig. 1. Schematic drawing of the gas distribution coupled with the calorimeter. HR = hydride reservoir, NV = needle valve, PtR = platinum resistance, th*i* = thermocouple *i* (only th1 is drawn, within the inner rod, the arrows indicate the position of th1, 2, 3 and 4).

sample holder that has very high thermal transfer capacity is made by superposition of 10 copper plates, giving an exchange surface area of 25.62 cm^2. The sample holder is fully embedded within 92 cm^2 surface covered by the heat flux sensors.

With regard to the thermopile, the reactor is an open system. Thus, it is important to detect all sources for heat transport through the gas phase, because we are concerned with the relevance of the heat measurement. In order to detect heat fluxes, fast response chromel–alumel thermocouples are mounted in the reactor. The thermocouples act as secondary thermal sensors, because they measure the time evolution of the temperature profile above the thermopile and, consequently, any perturbation in the thermal losses.

3.3. Sample

This research has been performed with two different batches of ZrNi. The first (sample 1) intentionally contained traces of cerium oxide (<1%) making it brittle. The second (sample 2) batch is an ingot of very high purity. Microprobe analysis of this high purity ZrNi did not show any significant impurities but some possible compositional inhomogeneities, e.g. traces of Zr_9Ni_{11}. X-ray diffraction did not show the presence of any other phases.

Investigations have been carried out successively at 116.3, 126.6, 152.6 and 191.2°C for sample 1 and at 210.6 and 226°C for sample 2. The experimental results subjected to the analysis concern activated materials. A detailed identification of the series with the thermodynamic paths followed during the processes of absorption and desorption can be found in [16].

4. Heat measurements

4.1. Calibration of the calorimeter

The amount of energy Q(J) dissipated by the reaction is given by

$$Q\,(\mathrm{J}) = k_c \times \int_0^t E(t)\,\mathrm{d}t \qquad (2)$$

where k_c represents the calibration coefficient and $E(t)$ the output signal of the thermopile. To calibrate over a wide range of pressure and temperature without perturbing the system, a platinum resistance (PtR) is mounted permanently within the reactor. The position of the PtR within the sample holder was determined once for all to correspond to the maximum sensitivity of the signal delivered by the thermopiles. However, the heat generated by Joule heating does not correspond exactly to the experimental conditions because the system is (i) in a static condition when performing calibration and also (ii) the heat is not generated within the sample itself. The latter influences only the shape of the signal [1], in the former case care must be taken for possible modification of the thermal losses during the reaction.

Extended analysis of the calibration coefficient was carried out with hydrogen gas in the presence of the

unactivated sample. It was established that k_c is independent of the pressure for the 100–50 kPa pressure range. Below 100 Pa, however, measurements indicate a large scatter in k_c which would introduce large errors into the thermodynamic parameters.

4.2. Heat transfer in the low pressure range

The sample holder is not in very good contact with the inner wall of the reactor because of the need for a minimum space for introduction of the container. Such a configuration makes the signal detected by the thermopile sensitive to the gas pressure because heat is transmitted through the walls both by the sample container and the hydrogen gas. During calibration, no gas flows in or out of the reactor and heat transfer through the gas phase remains in a steady state. Introduction (withdrawal) of the hydrogen gas must not modify the heat losses through the gaseous phase during the mass transfer otherwise erroneous heat determinations will be obtained despite the accuracy of the calibration coefficient. In spite of the precautions taken, using low mass flow and laminar flow, it is rather difficult to maintain steady state heat transfer through the gas phase because the thermal conductivity of the gas depends strongly on pressure and temperature. Fig. 2 shows the variation of the thermal conductivity of the hydrogen gas, λ_{H_2}, with the logarithm of the pressure according to Kennard [17] (see Appendix A). The sharp variation in the 'S' shaped curve is observed when the thermal conductivity of the gas diminishes markedly below $P \approx 10$ kPa. The influence of this effect on the heat measurements is evaluated by carrying out hydrogen absorption measurements across the pressure range of the molecular regime (Knudsen regime), i.e. from vacuum up to ~10/20 kPa.

4.3. Results

The system was operated as follows: every 2 h and half the same dose (for one series) of hydrogen gas was added (withdrawn) to (from) the sample. Thermograms obtained in the two phase region, corresponding to the formation of $ZrNiH_{3-\delta}$ are shown in Fig. 3. They represent typical calorimeter responses resulting from sequential additions of hydrogen from 116.3 to 210.6°C in the pressure range 50 Pa–20 kPa. Fig. 4 shows the variation of the temperature with time in the reactor for one representative experiment in the series.

Thermograms in Fig. 3a clearly show an endothermic contribution which disappears during the series at

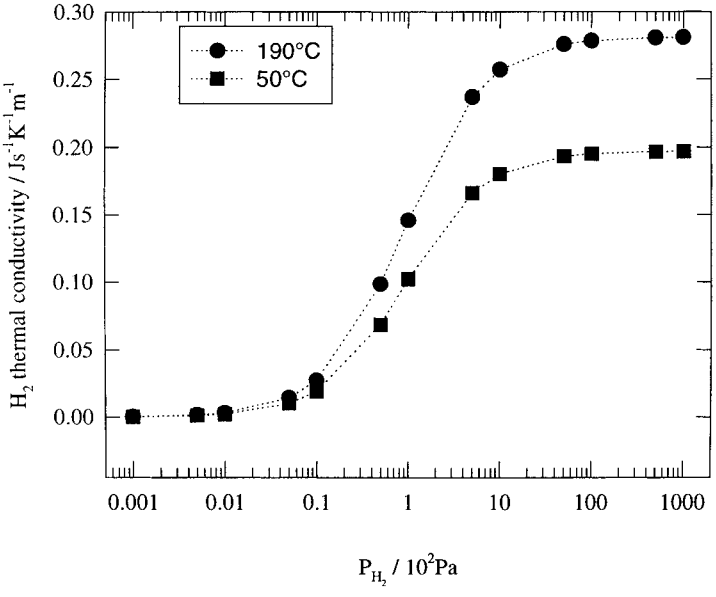

Fig. 2. Thermal conductivity of hydrogen gas vs. *P*.

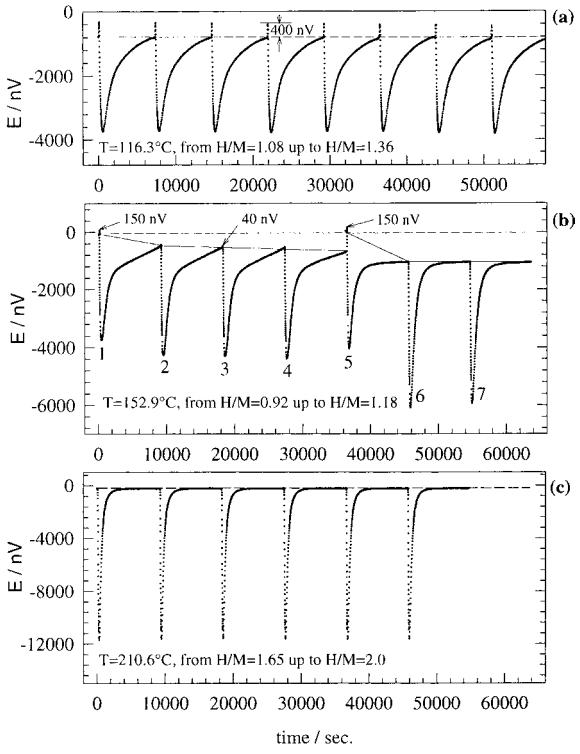

Fig. 3. The observed responses of the calorimeter for sequential additions of identical hydrogen doses. H_2 gas is (a) in the Knudsen regime, $P_{plat} \approx 300$ Pa; (b) reaching the end of the Knudsen regime, $P_{plat} \approx 1.5$ kPa; (c) in the classical regime, $P_{plat} \approx 15$ kPa.

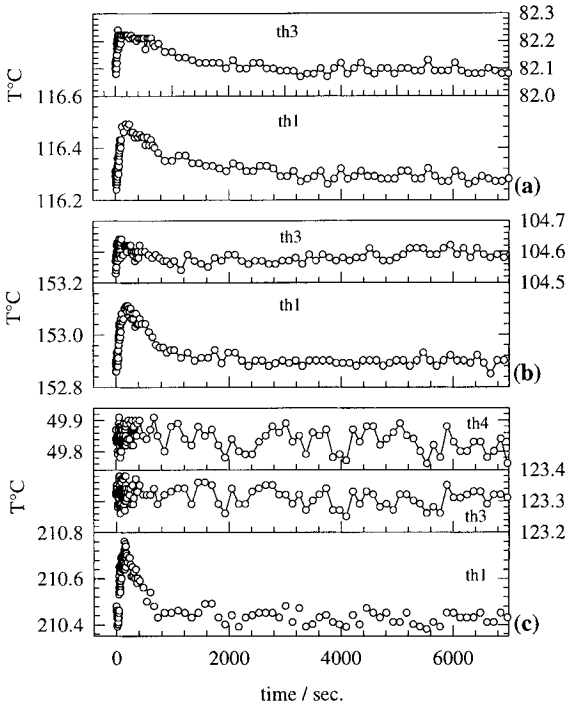

Fig. 4. Temperature variation inside the sample and above the thermopile, th1 = sample temperature, th3, th4 above thermopile, location can be seen on Fig. 1.

152.9°C (Fig. 3b, peak no. 6), and is not present at all at 210.6°C, (Fig. 3c). The presence of the endothermic deviation is correlated with changes of the heat flow process as proven by the corresponding temperature variations (Fig. 4a) above the thermopile. Under these circumstances only a part of the heat of reaction is detected by the thermopile. This configuration should correspond to the lower branch of the 'S' shaped curve (Fig. 2) where the thermal conductivity of the gas is almost nil. Here, the calibration coefficient is overestimated leading to erroneously large heats of reaction. When approaching the upper limit of the transition, the absence of an endothermal effect does not necessarily imply that redistribution of heat is not occurring, as for peak nos. 6 and 7 (Fig. 3b) with a corresponding plateau pressure of 1 kPa. Compared with Fig. 4a, the amplitude of the temperature variations in Fig. 4b is now smaller but remains significant such that the endothermal effect is masked by the reaction. Finally, at 210.6°C, according to the plateau pressure, $P = 20$ kPa, the system is not anymore in the Knudsen regime. The heat of reaction can be evaluated because the temperatures above the thermopile (Fig. 4c) are constant with typical fluctuations observed for convection in the gas phase. The baseline recovers its true equilibrium values after each absorption.

The results demonstrate that calorimetric measurements can be affected by artefacts which are experimentally identified by detecting the different sources of heat loss within the reactor. That is the only way to ascertain the accuracy of the thermodynamic parameters for gas–solid systems in the low gas pressure domain.

5. Modeling

To better understand the shape of the thermograms, simple models have been developed assuming firstly

that the heat transport inside the reactor occurs only along the *X*-axis, then assuming that a heat loss through the top of the thermopile occurs along the *Y*-axis.

5.1. Mono-dimensional case

5.1.1. Representation of the calorimeter cell

The development of the model is based on an equivalent system that is representative of the calorimeter cell shown in Fig. 1. The calorimeter cell arrangement is made of different concentric elements of known heat capacity and heat conductivity, in good or loose contact. Each interface represents an additional heat resistance. The reactor can be reduced to an equivalent system of three elements, as shown in Fig. 5:

1. The heat source (HS), which corresponds to the copper container and the sample.
2. The heat transfer domain reduced to a gaseous hydrogen film, the heat flux sensitive surface is provided by HS surface area.
3. The heat detector (HD), which includes the walls of the reactor and the thermopile.

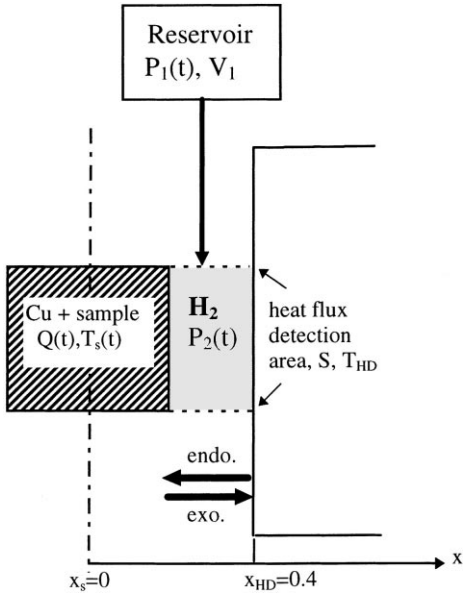

Fig. 5. Equivalent system representative of the calorimetric cell.

This simplification is justified by the fact that the only parameter under consideration is the thermal conductivity of the gas.

5.1.2. Physical description

When the reactor is under vacuum the thermal resistance between the sample holder and the heat detector is large and the sample temperature, T_s, is a few tenths of a degree lower than the temperature at the heat detector, T_{HD}. For this steady state, the baseline is shifted compared to the signal obtained with the true thermal equilibrium of the cell, e.g. $T_s = T_{HD}$. Thus, under vacuum, a small temperature gradient already exists between the sample and the heat detector and the inflow of hydrogen gas is beneficial to re-equilibrate the calorimeter cell. An endothermal signal is generated because heat must be supplied to the cell to adjust the temperatures. Simultaneously, the endothermal contribution is coupled with the exothermic contribution of the heat of transformation, driven by the amount of hydrogen absorbed by the sample and the modification of the thermal resistance in the gas phase. The in situ thermocouples allow measurement of the real time dependence of the temperature variation inside the reactor, but the temperature at the HD interface is not known exactly. Considering the large heat capacities of the furnace and the thermopile, the HD temperature will be determined by the thermocouple used for temperature regulation of the furnace, T_r. This thermocouple is located between the thermopile and the furnace. When the gas pressure is in the classical regime, the temperature readings indicate that $T_r = T_s = T_{HD}$, within the precision of the thermocouple.

The response of the calorimeter is modeled by assuming a temperature gradient between the sample and the heat detector. The pressures in the reference and reactor volumes, as well as sample temperature variation will be calculated and compared with the experimental data. This description is consistent with the following hypotheses:

1. At time $t = 0$, a temperature gradient exists between the heat source, $T_s(t)$, and the heat detector T_{HD}, that is considered as constant.
2. The temperature gradient is taken as linear due to the small thickness of the gaseous film.

3. The hydrogen mass transport for the transformation at the solid–gas interface is instantaneous all over the sample which means that $T_s(t)$ varies uniformly. This is justified by considering that the sample is equally distributed within the 10 copper plates.
4. The heat source is considered as a point (no spatial extension).

At this stage, the thermal losses along the vertical axis of the reactor are ignored, the cylindrical symmetry of the configuration allows a further simplification by solving the problem in one dimension.

5.1.3. Equations of the model

The above assumptions lead to the heat balance equation

$$\left(\frac{dQ}{dt}\right)^{\text{reaction}} + \left(\frac{dQ}{dt}\right)^{\text{leak}} = \left(\frac{dQ}{dt}\right)^{\text{capacity}} \tag{3}$$

The first term is the heat source. The second term represents the amount of heat which is dissipated through the gaseous film. The third one corresponds to the part of the heat which is accumulated, increasing the HS temperature. The resulting governing equation is

$$|\Delta_t H| \frac{dn_H(t)}{dt} - \lambda_{H_2} S \frac{\delta T(t)}{\delta x} = mC \frac{dT_s(t)}{dt} \tag{4}$$

where $\Delta_t H$ is the enthalpy for the transformation, dn_H the amount of hydrogen being absorbed, λ_{H_2} the thermal conductivity of the hydrogen gas, S the exchange surface area between HS and HD and mC the overall heat capacity of the sample and copper container. The assumption of the linear temperature gradient is reflected in the second term of Eq. (4) with

$$\delta T = T_{HD} - T_s(t), \quad \text{and} \quad \delta x = x_{HD} - x_s \tag{5}$$

At the heat detector, the heat flux will be given by

$$\left(\frac{dQ}{dt}\right)^{\text{HD}} = \left(\frac{dQ}{dt}\right)^{\text{leak}} \tag{6}$$

The mass balance for the reaction is

$$\frac{dn_1}{dt} = \frac{dn_2}{dt} + \frac{dn_H}{dt}, \tag{7}$$

where dn_1/dt corresponds to the mass of hydrogen transferred from the reference volume into the reactor, dn_2/dt, the number of moles accumulated in the reactor. The number of moles absorbed, dn_H/dt, satisfies the empirical rate equation derived from the Johnson–Mehl–Avrami equation [18] given by

$$\begin{cases} \dfrac{dn_H}{dt} = \delta\left(\dfrac{H}{M}\right) n_M \dfrac{d\alpha}{dt} \\ \dfrac{d\alpha}{dt} = k_r[P_2(t) - P_{equ}(t)](1 - \alpha(t))t^{N-1} \cdot N \end{cases} \tag{8}$$

with

$$\alpha(t) = \frac{H/M|_t - H/M|_{t=0}}{H/M|_{t=\infty} - H/M|_{t=0}},$$
$$\delta\left(\frac{H}{M}\right) = \left.\frac{H}{M}\right|_{t=\infty} - \left.\frac{H}{M}\right|_{t=0} \tag{9}$$

where $\delta(H/M)$ corresponds to the step in H/M for one experiment in the series, α the transformed fraction, k_r the rate constant, $P_2(t)$ and $P_{equ}(t)$ represent the time dependent pressure in the reference volume and the 'equilibrium' plateau pressure, respectively. Finally, N is a morphological parameter of the Johnson–Mehl–Avrami equation.

dn_1/dt is calculated by using the Poiseuille law [18] and the ideal gas law

$$\left.\frac{dP_1}{dt}\right|_t = \frac{k_v}{V_1}[P_1^2(t) - P_2^2(t)] \quad \text{and} \quad P_1 V_1 = n_1 R T_1 \tag{10}$$

$$\text{give} \quad \frac{dn_1}{dt} = \frac{V_1}{RT_1}\frac{dP_1}{dt} = \frac{k_v}{RT_1}[P_1^2(t) - P_2^2(t)] \tag{11}$$

where k_v characterizes the needle valve, P_1 and P_2, the pressure in the reference volume V_1 and the reactor V_2, respectively. Knowledge of dn_2/dt allows to calculate P_2 taking into account the temperature gradient in the reactor.

$$\left.\frac{dP_2}{dt}\right|_t = R\left[\frac{1}{\sum_j [dV_j \cdot 1/(T_{j+1} - T_j)\ln(T_{j+1}/T_j)]}\right]\frac{dn_2}{dt}, \tag{12}$$

where T_j is the temperature assigned to the element ΔV_j of the partitioned reactor volume [1].

5.1.4. Numerical applications

The set of differential equations given by the model are solved by a finite difference method using the

Table 1
Geometrical parameters

Reference volume	84.307 cm^3
Reactor volume	
Volume reactive cell, th1	13.965 cm^3
Volume between th1 and th2	10.055 cm^3
Volume between th2 and th3	10.272 cm^3
Volume between th3 and th4	7.000 cm^3
Volume between th4 and t_{room}	3.000 cm^3
Volume head	4.600 cm^3
Volume connecting tube	15.193 cm^3
δx, thickness gaseous film	0.4 mm
L_1	2.0 cm
L_2	4.0 cm
Sample container surface area	25.2 cm^2
$S_{SS} = S_{y1} = S_{y2}$	6 mm^2

Table 2
Thermophysical constants

k_v	2.7×10^{-11} ($m^3\ Pa^{-1}\ s^{-1}$)
$m_1 = m_{copper}$	63.32 (g)
C_{p1}(Cu)	$22.64 + 6.27 \times 10^{-3} \times T$ ($J^{-1}\ mol^{-1}\ K^{-1}$)
C_p(ZrNi)	214 ($J\ mol^{-1}\ K^{-1}$)
$m_2 = m_{fins}$	60.52 (g)
C_{p2}(SS)	0.477 ($J\ g^{-1}\ K^{-1}$)
$\lambda_{SS} = \lambda_{y1} = \lambda_{y2}$	26.0 ($J\ s^{-1}\ m^{-1}\ K^{-1}$)

appropriate boundary conditions

$$T_{HD} = T_{const},\ \ T_s(t=0) = T_s(t=\infty) = T_s^0,$$
$$T_1(t=0) = T_1^0,\ \ T_i(t=0) = T_i^0,\ \ P_1(t=0) = P_1^0,$$
$$P_2(t=0) = P_2^0,\ \text{ and }\ \alpha(t=0) = 0,\ \ \alpha(t=\infty) = 1$$

The parameter values used in the simulation are listed in Tables 1–3.

First of all, the response of the calorimeter is calculated to test the sensitivity of the model with regards to different initial values of the temperature gradient, δT, and with regards to the thermal capacity of the container, mC, as well as to different values of the initial pressure. When the system is in the two phase region at a pressure $P =$ constant within the Knudsen domain, a hydrogen dose is fully absorbed by the sample. It can be seen in Fig. 6a that the largest endothermal effect is obtained with $\delta T = 1$ K. Such a signal has been observed experimentally for the first hydrogen absorption when the reactor at time $t = 0$ was under vacuum. In this case, the major contribution of the heat flux converges inward to the container to re-equilibrate the temperature. It is accompanied by a permanent base line shift toward a new steady state. In the subsequent absorptions, δT will progressively diminishes to fall below 0.1°C, as long as the hydrogen gas remains in the Knudsen domain to reach finally the true equilibrium value in the classical regime, e.g. $T_s = T_{HD}$. This situation accounts partly for the thermograms of Fig. 3b.

Keeping $\delta T = 0.1$ K, the thermal capacity has been divided by two and Fig. 6b shows that correspondingly the contribution of the endothermic effect diminishes, since at the first stage less heat is required to compensate the initial δT. Finally, in Fig. 6c, for increasing initial pressure, the correlation between thermal conductivity of the gas and pressure is evidenced by the progressive disappearance of the endothermal contribution.

Results of the simulation of the global system variables, heat flux, P_1, P_2, T_s are plotted in Fig. 7 for one representative experiment of the 116.3°C

Table 3
Experimental parameters for the different temperatures

	$T = 116.3$°C	$T = 152.9$°C	$T = 226.2$°C
k_c	0.4	1.32	1.2
N	0.78	0.74	0.78
ΔH/M	0.0378	0.0427	0.0585
Q (J)	31.0	34.91	45.1
P_1^0 (Pa)	13730	16720	49760
P_2^0 (Pa)	0	1720	30600
P_{equ} (Pa)	0	1700	30500
δT_{init} (K)	0.05	0.01	0.00
$\lambda^*_{H_2}$ ($J\ s^{-1}\ m^{-1}\ K^{-1}$ (1 bar))	0.224	0.241	0.272

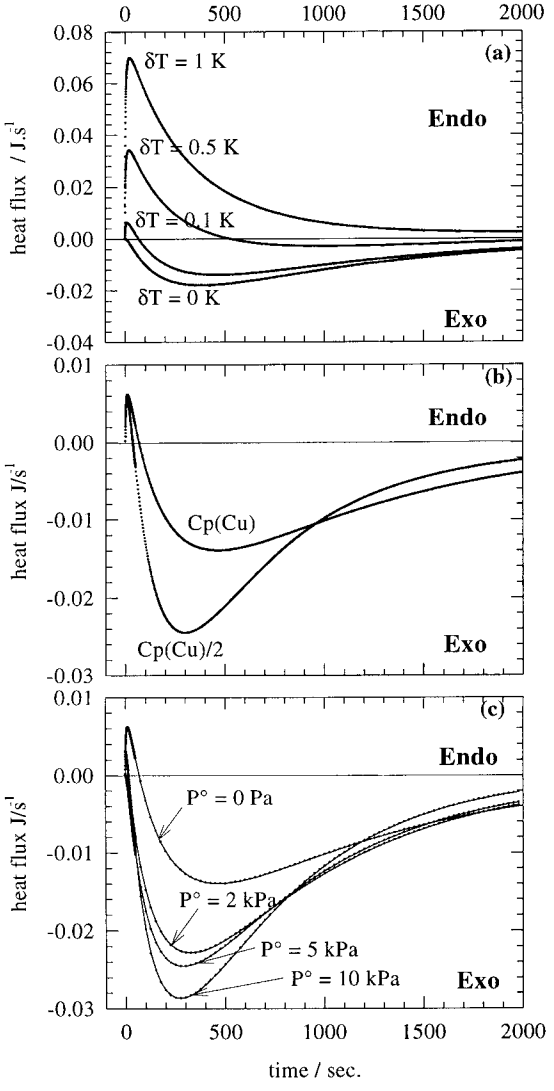

Fig. 6. Calculated thermograms demonstrating the influence of (a) initial temperature gradient; (b) heat capacity contribution of the sample container; (c) initial gaseous pressure in the reactor.

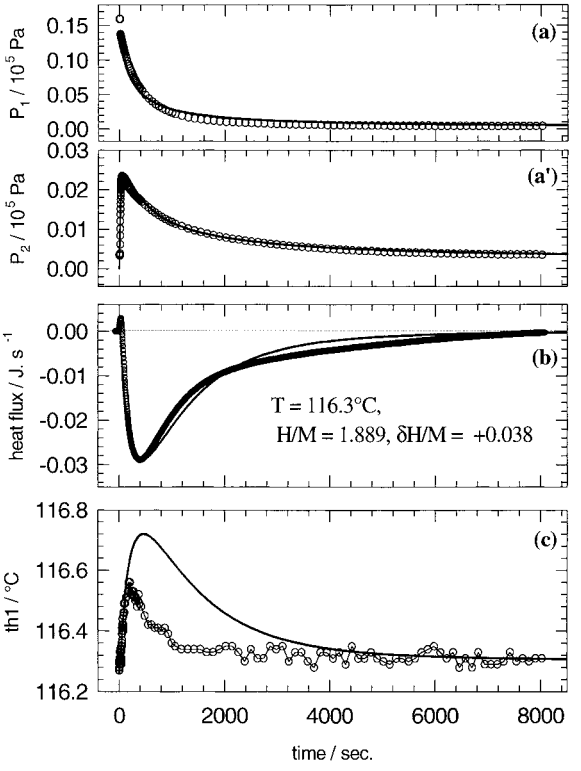

Fig. 7. Comparison measurements (symbols)/model (lines): (a) pressure in V_{ref}; (a′) pressure in reactor; (b) thermogram; (c) sample temperature.

series. The experimental data correspond to the hydrogen absorption for a step in H/M of 0.039 with the initial 1.889 H/M. The calculated pressures, Fig. 7a–a′, reproduce quite accurately the experimental variations, justifying the choice of the rate equation. Comparison between the shape of the simulated and experimental thermograms, Fig. 7b, shows that a very good agreement is obtained up to 400 s, duplicating the shape of the endothermal effect. For comparison, the original signal of the calorimeter, expressed in nV, has been converted in $J\,s^{-1}$ using the calibration constant, k_c. Thus, the measured heat of transformation gives $\Delta_t H = -61$ kJ $(\text{mol H})^{-1}$, a value that is much more exothermic than the true value, $\Delta_t H = -34$ kJ $(\text{mol H})^{-1}$ [15,16]. When using the former quantity in the simulation, it is not surprising to find reasonable similarity between the calculated and experimental thermograms. At that point, the model does not prove that k_c is not valid for the dynamic conditions of hydrogen transfer. The results only confirm that the parameters used for λ_{H_2} governing heat transfer through the gas phase are satisfactory. Finally the calculated sample temperature T_s and the measured sample temperature are reported in Fig. 7c indicating the presence of a marked discrepancy between them. The calculated temperature is too high,

$\sim$0.16°C at the maximum. This suggests that the heat of transformation used for the calculation is too large and as a consequence shows that, now, k_c is not valid for the given experimental conditions.

In the low pressure range, assuming a temperature gradient between the heat detector and the sample container, the model can generate endothermal effects. The shape of the signal detected is weighted by the heat transfer in the gas phase and consequently by the thermal conductivity of the hydrogen gas. At the beginning of the hydrogenation, e.g. for the first few experiments, it is clear that enthalpies measured are wrong because the measuring sensor is completely perturbated, reaching a new steady state regime for each increment of hydrogen. In the low pressure range, the mono-dimensional model is relatively correct to interpretate the observed thermograms. However, when the pressure slowly increases the temperature gradient diminishes as well as the endothermal contribution and the model is no longer appropriate to simulate all the different experimental quantities, heat flux, P_1, P_2, T_s. As seen in Fig. 4, the temperature variation above the container becomes smaller and the disappearance of the endothermic effect, Fig. 3, does not necessarily imply the validity of the heat measurements. Heat leak trough the vertical axis of the thermopile must be included.

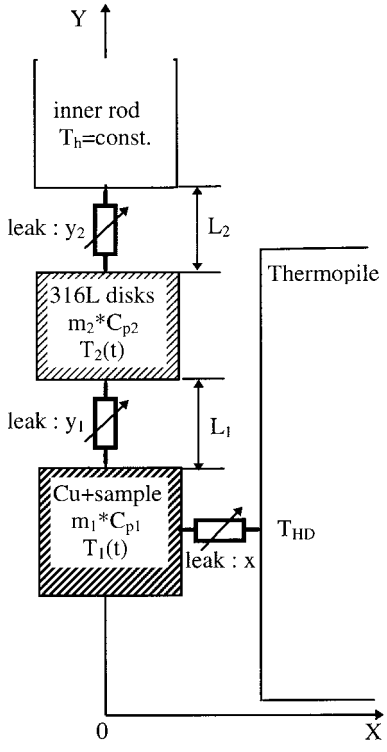

Fig. 8. Modified version of the equivalent system of Fig. 4 taking into account the vertical heat loss.

5.2. Bi-dimensional case

5.2.1. Physical description and equations

To take into account the heat loss in the *Y*-direction, the equivalent model system is modified as shown in Fig. 8. In the new configuration, the first heat leak occurs between the sample container at $T_1(t)$ and the equivalent representation of the stainless steel fins at $T_2(t)$. The second contribution is concerned by the leak between the fins and the inner rod at temperature T_h = constant. Along the vertical path, heat transfers between the elements through the guides which are used to support the container and the fins. The modification requires new expressions of the thermal balance, which has to be evaluated at the sample container,

$$\left(\frac{dQ}{dt}\right)^{\text{reaction}} + \left(\frac{dQ}{dt}\right)^{\text{leak},x} + \left(\frac{dQ}{dt}\right)^{\text{leak},y1} = \left(\frac{dQ}{dt}\right)^{\text{capacity}} \tag{13}$$

and at the fins levels,

$$\left(\frac{dQ}{dt}\right)^{\text{leak},y1} + \left(\frac{dQ}{dt}\right)^{\text{leak},y2} = \left(\frac{dQ}{dt}\right)^{\text{capacity}} = m_2 \cdot Cp_2 \frac{dT_2(t)}{dt} \tag{14}$$

$$\text{with :} \quad \left(\frac{dQ}{dt}\right)^{\text{leak},y1} = \lambda_{SS} \cdot S_1 \frac{[T_1(t) - T_2(t)] - [T_1^0 - T_2^0]}{L_1} \tag{15}$$

$$\text{and} \quad \left(\frac{dQ}{dt}\right)^{\text{leak},y2} = \lambda_{SS} \cdot S_2 \frac{[T_2(t) - T_h(t)] - [T_2^0 - T_h]}{L_2} \tag{16}$$

Eqs. (15) and (16) indicate that the vertical leak is induced by the difference between the temperature gradient taken at time *t* and the corresponding value in

the steady state, e.g.

$$T_1(t=0) = T_1(t=\infty) = T_1^0 \quad \text{and}$$
$$T_2(t=0) = T_2(t=\infty) = T_2^0$$

5.2.2. Numerical applications

Simulations have been made for one representative experiment of the series carried out at 152.9°C, where the gaseous pressure is in the Knudsen domain and at 226.2°C where gaseous pressure is in the classical regime. Results are plotted in Figs. 9 and 10 for the 152.9 and 226.2°C studies, respectively.

The overall rate law is obviously not affected by taking into consideration the heat leak through the vertical axis. Hence, the calculated pressures agree with the experimental values, Figs. 9a–a′ and 10a–a′.

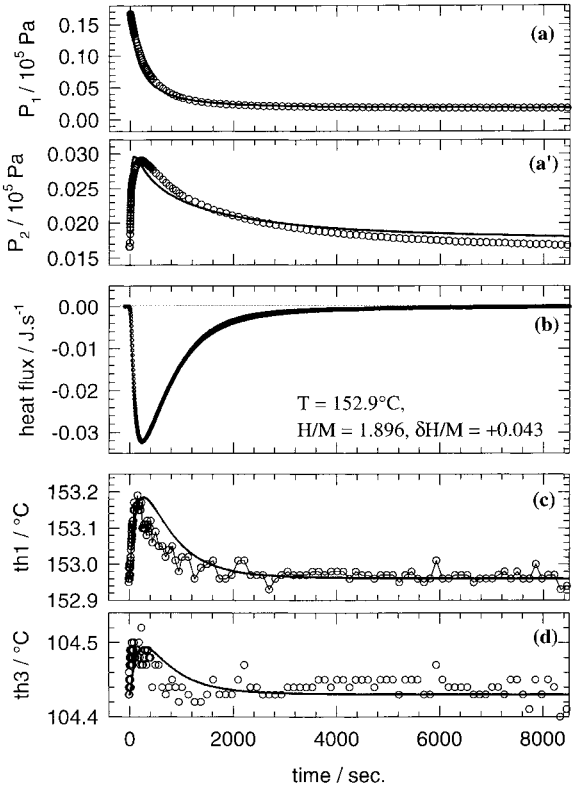

Fig. 9. $T = 152.9$°C, comparison measurements (symbols)/model (lines): (a) pressure in V_{ref}; (a′) pressure in reactor; (b) thermogram; (c) th1 = sample temperature; (d) th3 = temperature above thermopile.

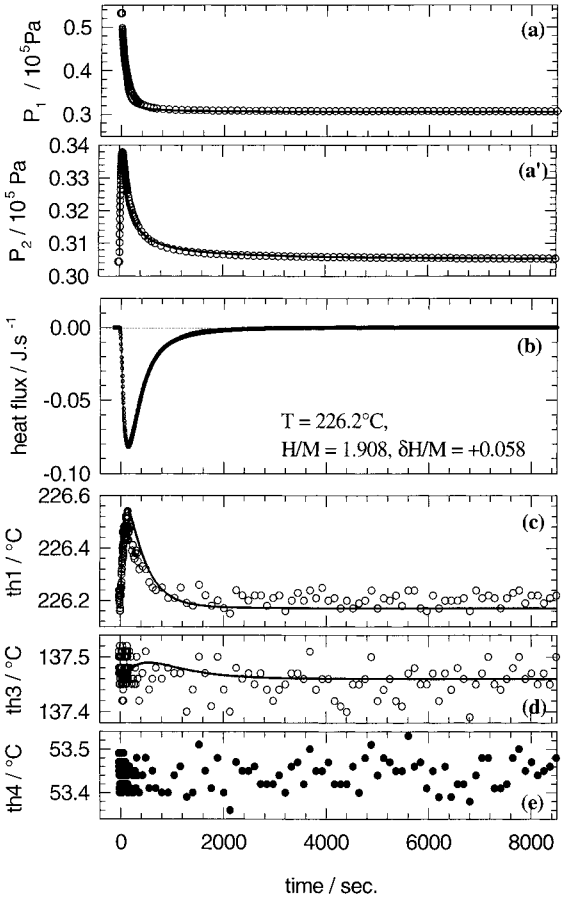

Fig. 10. $T = 226.2$°C, comparison measurements (symbols)/model (lines): (a) pressure in V_{ref}; (a′) pressure in reactor; (b) thermogram; (c) th1 = sample temperature; ((d)–(e)) th3, th4 = temperatures above thermopile.

The model is furthermore able to reproduce the experimental thermograms excellently, Figs. 9b and 10b. It must be pointed out that at 152.9°C, despite the fact that the system is in the Knudsen region, the endothermal contribution is quickly overcome by the heat of transformation and the model follows that behavior.

The final test on the validity of the model is provided by the calculated temperatures within the sample and above the thermopile. Although the temperature variations remain small (of the order of 0.3 and 0.15°C for the sample and the thermocouple located above the thermopile, respectively), the

calculated and measured maximum temperature increase of the sample gives now the same value, Fig. 9c. However, when the sample temperature decreases, a slight discrepancy is observed, 0.06°C between the calculated and measured values. This behavior is also reproduced for the thermocouple located above the thermopile, Fig. 9d. At 226.2°C the agreement between calculated and measured temperatures is even better, demonstrating that the model is sensitive enough to simulate all the parameters of the system and is able to take into account the changes of the heat losses above the thermopile.

6. Enthalpies

A judicious instrumentation of the calorimeter allowed us to determine the influence of the thermal conductivity of the hydrogen gas on the heat measurements in the low pressure domain. This makes a critical analysis of the heat evolved for the ZrNi–H_2 system possible. Complementary simulations using simple models confirm changes in the heat transfer paths through the gas phase. Thus, the enthalpies can be derived only from the 210.6 and 226.1°C data, when the temperature gradient above the heat detector is not influenced by the hydrogen mass transfer and remains constant, corresponding to a gaseous pressure above the Knudsen domain.

Although a detailed analysis of the thermodynamic and microstructural properties of the system is given elsewhere [16,19], we summarize here the main results. The average values of the relative enthalpies for $\beta \rightarrow \gamma$ transformation, trihydride formation, and $\gamma \rightarrow \beta$, trihydride decomposition are $\Delta_f H = -34.3 \pm 0.5$ kJ (mol H)$^{-1}$ and $\Delta_d H = 34.4 \pm 0.5$ kJ (mol H)$^{-1}$. The hydride decomposition enthalpy is equal, within experimental uncertainty, to the formation enthalpy. This is an important observation because the system has a large hysteresis. The hydride formation enthalpy measured calorimetrically at 50°C [15] is -34.0 ± 0.45 kJ (mol H)$^{-1}$. In view of these results, one can conclude that there is no significant temperature dependence of the enthalpy over a range of 180°C, implying that over that range, the summation of the heat capacity contributions cancel out and changes in the β, γ compositions over this range have negligible effect.

7. Conclusions

In this study, we have analyzed the validity of the enthalpy determinations for the reaction of H_2(g) with ZrNi. It has been shown experimentally and confirmed by modeling of the calorimeter cell, that as long as the hydrogen gas remains within the Knudsen regime, the heat measurements are invalid and lead to misinterpretation of the data. This problem is a very general one, which can be observed in any other solid/gas system in the low pressure range such as metal oxide/oxygen(g), and is also relevant in heat of adsorption measurements in porous systems. In this work, heat measurements become meaningful at 210°C.

Important fundamental results concerning the thermodynamics of metal hydride systems have been obtained. It should be pointed out that the hydride formation and decomposition enthalpies are equal in magnitude for a specific system, which has a large hysteresis. Moreover, within experimental uncertainty, there is no significant temperature dependence of the enthalpy of transformation over a range of 180°C.

Acknowledgements

The authors thank Prof. T.B. Flanagan (University of Vermont, USA) for criticisms and judicious discussion and R.C. Bowman Jr. (JPL, CA, USA) for providing us a sample of closely stoichiometric ZrNi of high purity.

Appendix A.

The thermal conductivity of gases is represented by two different expressions depending on the value of the a-dimensional Knudsen number defined as $k_N = \delta/d$, where δ is the mean free path of the molecule and d the distance between two parallel plans between which heat conduction occurs.

When $k_N \ll 1$, the kinetic theory of gases predicts that the thermal conductivity is independent of the pressure and Kennard [17] obtained the following expression:

$$\lambda_g = \tfrac{1}{4}(9\gamma - 5)\eta C_v, \quad \text{(A1)}$$

where C_v is the specific heat of the gas, η the viscosity and $\gamma = C_p/C_v$.

In the low pressure domain, $k_N \gg 1$, the thermal conductivity of the gas is a function of the pressure and of the nature of the gas through

$$\lambda_g^* = \frac{\lambda_g}{1 + k/d \cdot P_{gas}} \quad \text{and} \quad k = 2g \cdot \delta \cdot P_{gas} \qquad \text{(A2)}$$

where λ_g^* and λ_g are the pressure dependent and independent thermal conductivity, respectively. $\delta \cdot P_{gas}$ is a characteristic of a gas and is independent of the pressure. For hydrogen, $\delta \cdot P_{gas} = 117.7$ mm mbar; g is the temperature jump distance defined as

$$g = \frac{2 - a}{2a} \cdot \frac{9\gamma - 5}{\gamma + 1}$$

a is the accommodation factor whose value is between 0 and 1 depending on the nature of the gas.

References

[1] P. Dantzer, P. Millet, Rev. Sci. Instrum. 71 (2000) 142.
[2] S.L. Randzio, J.P. Grolier, J.R. Quint, Rev. Sci. Instrum. 65 (1994) 960.
[3] V. Torra, H. Tachoire, Thermochim. Acta 203 (1992) 419.
[4] J.F. Fernandez, F. Cuevas, C. Sanchez, J. Alloys Comp. 298 (2000) 244.
[5] V. Torra, H. Tachoire, J. Thermal Anal. 52 (1998) 663.
[6] W. Hemminger, G. Höhne, Calorimetry — Fundamentals and Practice, Verlag Chemie, Berlin, 1984.
[7] W. Zhang, M.P.S. Kumar, A. Visintin, S. Srinivasan, H.J. Ploehn, J. Alloys Comp. 242 (1996) 143.
[8] K. Watanabe, K. Tanaka, M. Matsuyama, K. Hasegawa, Fusion Eng. Design 18 (1991) 27.
[9] N. Mitsuishi, S. Fukada, N. Tanimura, J. Less Common Met. 123 (1986) 65.
[10] R.C. Bowman, P.B. Karlmann, S. Bard, Brilliant Eyes Ten-Kelvin Sorption Cryocooler Experiment (BETSCE), Final Report, JPL Publication 97-14, 1997.
[11] G.G. Libowitz, H.F. Hayes, T.R.P. Gibb, J. Phys. Chem. 62 (1958) 76–79.
[12] M.E. Kost, L.N. Padurets, A.A. Chertkov, V.I. Mikheeva, Russian J. Inorg. Chem. 25 (1980) 471 (translated from Zhurnal Neorganicheskoi Khimii 25 (1980) 847).
[13] D.G. Westlake, H. Shaked, P.R. Mason, B.R. McCart, M.H. Mueller, J. Less Common Met. 88 (1982) 17.
[14] M. Gupta, J. Alloys Comp. 293–295 (1999) 190.
[15] W. Luo, A. Craft, T. Kuji, H.S. Chung, T.B. Flanagan, J. Less Common Met. 162 (1990) 251.
[16] P. Dantzer, P. Millet, T.B. Flanagan, Met. Mater. Trans. A 31 (2000).
[17] E.H. Kennard, Kinetic Theory of Gases, McGraw-Hill, New York, 1938.
[18] H.Y. Cai, P. Millet, P. Dantzer, J. Alloys Comp. 231 (1995) 427.
[19] N. Michel, S. Poulat, P. Millet, P. Dantzer, L. Priester, M. Gupta, J. Alloys Comp., submitted for publication.